Science Of The Total Environment
May 2024, Volume 924 Pages 171365 (15p)
https://doi.org/10.1016/j.scitotenv.2024.171365
https://archimer.ifremer.fr/doc/00941/105263/

Can three-dimensional nitrate structure be reconstructed from surface information with artificial intelligence? - A proof-of-concept study

Yang Guangyu Gary [1], Wang Qishuo [1], Feng Jiacheng [1], He Lechi [1], Li Rongzu [1], Lu Wenfang [1, 2, *],
Liao Enhui [3], Lai Zhigang [1, 2]

[1] School of Marine Sciences, Sun Yat-Sen University, Zhuhai, Guangdong, China
[2] Southern Marine Science and Engineering Guangdong Laboratory (Zhuhai), Zhuhai 519000, China
[3] School of Oceanography, Shanghai Jiao Tong University, Shanghai 200030, China

* Corresponding author : Wenfang Lu, email address : luwf6@sysu.edu.cn

Abstract :

Nitrate is one of the essential variables in the ocean that is a primary control of the upper ocean pelagic ecosystem. Its three-dimensional (3D) structure is vital for understanding the dynamic and ecosystem. Although several gridded nitrate products exist, the possibility of reconstructing the 3D structure of nitrate from surface data has never been exploited. In this study, we employed two advanced artificial intelligence (AI) networks, Unet and Earthformer, to reconstruct nitrate concentration in the Indian Ocean from surface data. Simulation from an ecosystem model was utilized as the labeling data to train and test the AI networks, with wind vectors, wind stress, sea surface temperature, sea surface chlorophyll-a, solar radiation, and precipitation as the input. We compared the performance of two networks and different pre-processing methods. With the input features decomposed into climatology and anomaly components, the Earthformer achieved optimal reconstruction results with a lower normalized mean square error (NRMSE = 0.1591), spatially and temporally, outperforming U-net (NRMSE = 0.2007) and the climatology prediction (NRMSE = 0.2089). Furthermore, Earthformer was more capable of identifying interannual nitrate anomalies. With a network interpretation technique, we quantified the spatio-temporal importance of every input feature in the best case (Earthformer with decomposed inputs). The influence of different input features on nitrate concentration in the adjacent Java Sea exhibited seasonal variation, stronger than the interannual one. The feature importance highlighted the role of dynamic factors, particularly the wind, matching our understanding of the dynamic controls of the ecosystem. Our reconstruction and network interpretation technique can be extended to other ecosystem variables, providing new possibilities in studies of marine environment and ecology from an AI perspective.

Graphical abstract

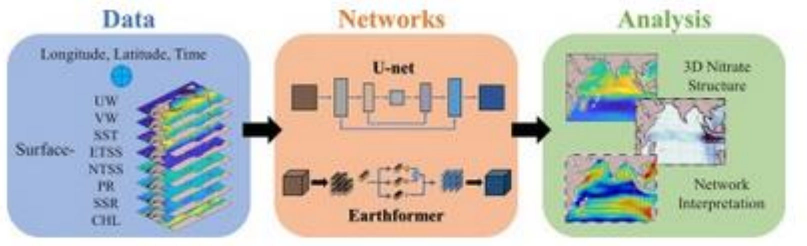

Highlights

► Two advanced AI networks were applied in reconstructing 3D structure of nitrate from surface data ► A deep learning interpretation technique was used to explain the spatio-temporal influence of each input feature ► Networks can achieve high accuracy and capture interannual nitrate anomalies, reflecting its dynamic control

Keywords : Nitrate, Indian Ocean, Artificial intelligence, Three-dimensional reconstruction

1. Introduction

Nitrate is one of the essential climate variables, plays a crucial role in characterizing the ecosystem and climate system (https://gcos.wmo.int/en/essential-climate-variables). Nitrogen limitation often links to phytoplankton productivity and carbon fixation via photosynthesis (Bristow, Mohr, Ahmerkamp, & Kuypers, 2017), particularly for our region of interest, the Indian Ocean (Y. Dai, Cao, & Wang, 2020). As a fundamental component of the nitrogen cycle, nitrate is regulated by both oceanic biogeochemical and physical processes, including its responses and feedback to climate changes (Voss et al., 2013). Specially, the biogeochemical processes such as biological uptake and remineralization, as well as nitrate reduction to ammonium or nitrification transfer different species of nitrogen (Hutchins & Capone, 2022). In general, nitrate concentration is lower in the euphoric layer due to the high efficiency of phytoplankton, while higher concentration is in the deep layer since the regeneration in subsurface oceanic regions through the activity of remineralization. Physically, such vertical gradients imply that vertical processes that can move nutrient beneath the nutricline to the euphotic zone are the key physical regulators of productivity. These processes range from wind-driven coastal upwelling in the ocean boundary (Bakun, 1973; W. Lu et al., 2018) to mixing processes (Behrenfeld, 2010) that are ubiquitous in the surface ocean.

The ocean nutrients were widely measured (Talley et al., 2016); however, due to the labor-intensive and costly nature of in-situ observation, they remain largely undersampled Du et al. (2021). Synthesis efforts mapping from discrete profiling data yielded gridded data products (Are Olsen et al., 2020), which was applied in many studies (M. Dai et al., 2023). These gridded products can support model simulating and understanding the biogeochemical system in many oceans, including the Indian Ocean (Raddatz et al., 2023). With the support of gridded nutrient products as the initial and/or boundary condition for configuring a physical-biogeochemical coupled model (W. Lu et al., 2018; Z. Lu, Gan, Dai, Zhao, & Hui, 2020), a variety of biogeochemical reanalysis products were enabled, such those on the Copernicus Marine Service data center. Yet, reanalysis models are expensive to run or complex to configurate, and hence are also very limited. At present, gridded nutrient products, such as the World Ocean Atlas (Garcia, Boyer, Locarnini, Baranova, & Zweng, 2018) or the Global Ocean Data Analysis Project (GLODAP, Are Olsen et al., 2020), can only achieve a 1-degree climatology resolution. Thus, using diverse techniques to reconstruct the three-dimensional structure of nutrient concentration is of great scientific interest and relevance. AI might be the solution, as it demonstrates significant potential in numerical simulation and forecasting oceanic phenomena (Dong et al., 2022; Sonnewald et al., 2021).

For nutrient reconstruction, most existing studies are limited to indirect empirical estimates, as no special electromagnetic or optic signatures could be used for direct remote sensing. A first endeavor in estimating nitrate through satellite imagery was made as early as 1999 (Goes, Saino, Oaku, & Jiang, 1999), which reconstructed the global surface nitrate in discrete months. In 2014, attempts were made to reconstruct time series of surface nitrate concentrations (Arteaga, Pahlow, & Oschlies, 2015). Recently, as a pioneer study for interior nutrient reconstruction, Du et al. (2021) applied an empirical relationship between in-situ temperature and salinity to reconstruct the 3D nutrient concentration in the South China Sea. L. Wang et al. (2023) trained a deep network to reconstruct the nitrite field using 3D temperature and salinity in the open Pacific, showing a good performance. Their studies, however, merely prove the feasibility of climatology monthly nutrient structure, leaving the multiyear monthly reconstruction problem open to be answered.

Ocean remote sensing can observe the large-scale surface of the ocean. However, due to the limitation of remote sensing techniques, it is unable to directly observe the interior of the ocean. Since the 2010s, the subsurface and Deep Ocean Remote Sensing (DORS) technique (Klemas & Yan, 2014) has become a hot field of ocean remote sensing, which is defined as the indirect reconstruction of the ocean interior through surface remote sensing data. The DORS technique was broadly applied in ocean big-data reconstruction problems of ocean physics, e.g., ocean heat content (W. Lu & Su, 2023), subsurface temperature anomalies (W. Lu, Su, Yang, & Yan, 2019; Su, Zhang, Lin, Lu, & Yan, 2021; K. Zhang, Geng, & Yan, 2020), and temperature-salinity structures (Guinehut, Dhomps, Larnicol, & Le Traon, 2012). In recent years, Artificial intelligence (AI) has emerged as a remarkable method (Dong et al., 2022), providing revolutionized solutions for various non-linear regression problems (Ding, Chen, Lu, & Wang, 2021; Su, Lu, et al., 2021; Zhou, Lu, Chen, & Li, 2023), as well as the DORS reconstruction problems, e.g., Su, Jiang, Wang, Zhuang, and Yan (2022) utilized ConvLSTM for subsurface temperature reconstruction. In addition, the DORS reconstruction was also boosted by the availability of big ocean data. To date, little attention has been paid to reconstructing the biogeochemical variables, such as the nutrients, in particular, nitrate concentration, from the perspective of DORS. Our main purpose of this study is to bridge this gap.

The Indian Ocean (See Figure 1) is an ideal region for conducting comprehensive investigations, characterized by its complex dynamics and interactions with large-scale climate drivers, including monsoons, the Indian Ocean Dipole (IOD), and the El Niño-Southern Oscillation (ENSO). During summer monsoon, the high temperatures cause an increase in warm and moisture-laden air over the ocean, resulting in abundant rainfall. In contrast, the cold winter monsoon causes a decrease in humidity over the ocean, leading to reduced precipitation (Schott & McCreary, 2001). The monsoonal variations play a crucial role in regulating ecosystem processes, through the modulation of physical nutrient supply mechanisms, such as upwelling, vertical mixing, precipitation and river discharges (Koné, Aumont, Lévy, & Resplandy, 2009; Rixen, Gaye, & Emeis, 2019). On the other hand, climate drivers such as IOD and ENSO modulate these processes. During positive IOD and ENSO events, atmospheric convection over the Indian Ocean is suppressed, resulting in increased solar radiation and subsequent warming of the ocean (Neelin et al., 1998; Su, Wei, Lu, Yan, & Zhang, 2023). Furthermore, the strengthening of southeast trade winds in the eastern Indian Ocean during these events enhances surface evaporation, oceanic vertical mixing, and coastal upwelling (Tokinaga & Tanimoto, 2004), leading to the redistribution of nutrients throughout the region. Other dynamic mechanisms also have an impact on the ecological environment and nutrient distribution in the Indian Ocean. For instance, during the upwelling period in the Arabian Sea, physical driving factors contribute to the enrichment of surface nutrients, leading to anomalous changes in nutrient concentrations (Seelanki, Nigam, & Pant, 2022; Shafeeque et al., 2019).

In summary, to prove the concept that 3D nitrate structure can be reconstructed from surface data, we chose two different AI algorithms, U-net and Earthformer. U-net is a modified convolutional neural network that incorporates residual connections. Initially, it was used for biomedical image segmentation (Ronneberger, Fischer, & Brox, 2015). Given its excellent feature extraction capability, U-net has been widely applied in AI oceanography studies (X. Li et al., 2020, and reference therein). For example, it has been used for eddy identification based on satellite remote sensing images (Saida & Ari, 2022; Zhao, Huang, Yang, Radenkovic, & Chen, 2023), sea surface salinity prediction (Huarong Xie, Xu, Cheng, Yin, & Fan, 2023; Xuewei Zhang, Zhao, & Han, 2023), and sea surface temperature forecasting (Sun, Zhou, Li, & Zhou, 2022; Taylor & Feng, 2022; H. Xie, Xu, Cheng, Yin, & Jia, 2022). On the other hand, Earthformer is an advanced artificial neural network based on Transformer in the field of Earth sciences, recently proposed for spatiotemporal prediction problems (Gao et al., 2022).

In this study, we aim to prove the concept of DORS for nitrate concentration with AI. In Section 2, we first introduce the data and methodology employed in this study. In Section 3, we evaluate the performance of the networks using statistical metrics and showcase the response of networks to anomalous climatic conditions. We also use a statistical method to interpret the trained network and to discover the underlying controls of nitrate structure in a representative sea. We discuss the limitations and potential of our reconstruction in Section 4. In Section 5, conclusions are provided.

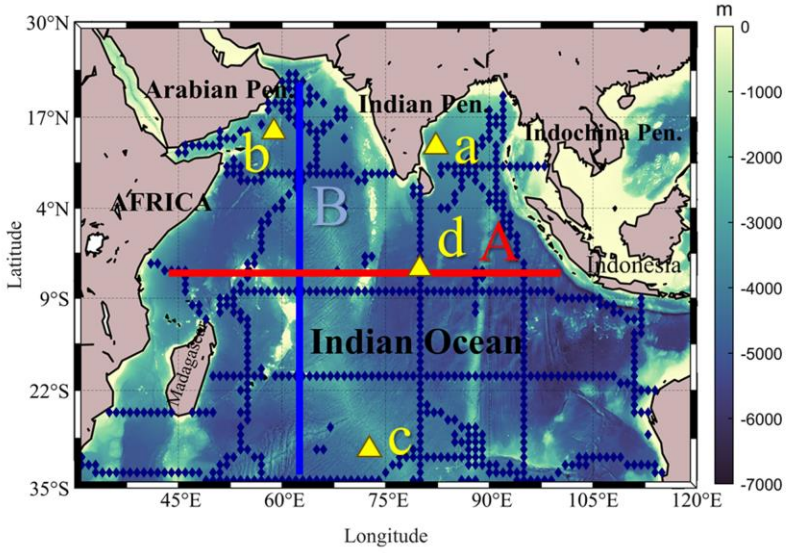

Figure 1. Bathymetry of the Indian Ocean and its adjacent regions. Markers and lines are

selected locations for illustrating the vertical distribution of nitrate concentration in section 3. Showing are Site a: Bay of Bengal (85°E, 15°N), Site b: Arabian Sea (61°E, 17°N), Site c: South Indian Ocean (75°E, 30°S), Site d: central basin (80°E, 5°S), Transection A (at 7°S), and Transection B (at 64°E). Blue markers in diamond shape represent the observed values obtained during the cruise selected in section 4.

2. Data and methods

2.1 Data

Since the long-term spatiotemporal product of nitrate is currently unavailable, we instead use a well-optimized biogeochemical model data as the training, validation, and testing data. This modeling system adopted the Nucleus European Modeling of the Ocean (NEMO, Madec, 2008) forced with the European Center for Medium Weather Forecast (ECMWF) atmospheric forcing, while the biogeochemical model was from Pelagic Interaction Scheme for Carbon and Ecosystem Studies (PISCES, Aumont, C., Tagliabue, Bopp, & Gehlen, 2015). The NEMO-PISCES system has high-quality data and was applied in various biogeochemical studies (Guieu et al., 2014; Keerthi et al., 2017; Person et al., 2019; T. Wang et al., 2021), justifying its application as the training data. The data were 0.25°×0.25° grided data obtained from the Copernicus Marine Services website at https://data.marine.copernicus.eu/product/GLOBAL_MULTIYEAR_BGC_001_029. The nitrate data contains 75 vertical levels, while the upper 42 levels (0-680 m) were used.

For the input features, various environmental factors can influence the distribution of nitrate. Singh and Ramesh (2015) identified sea surface temperature and solar radiation as important factors for explaining nitrate changes associated with primary production (F. Li et al., 2023). Singh, Gandhi, and Ramesh (2012) estimated the annual nitrate flux of 1.095 mmol m^{-2} yr^{-1} due to rainfall in the central Arabian Sea, indicating precipitation is an important feature. Additionally, the process of seawater convection driven by surface wind stress also has a notable impact on nitrate distribution (Lahiri & Vissa, 2022). Surface chlorophyll-a (CHL) is also chosen, as it reflects the biogeochemistry and is ample in terms of data sources (Das, Chakrabarty, Goswami, Basu, & Chaudhuri, 2019). Unlike prior studies that used 3D thermohaline data as major inputs (L. Wang et al., 2023), only using surface data can lead to better availability to reconstruct the historical nitrate structure, since historical 3D thermohaline data are also limited while surface data can be observed from remote sensing.

Based on these previous studies, the surface data we used in our research includes 10m u-component of wind (UW), 10m v-component of wind (VW), sea surface temperature (SST), mean eastward turbulent surface stress (ETSS), mean northward turbulent surface stress (NTSS), mean total precipitation rate (PR), surface net solar radiation (SSR), and surface CHL. The UW, VW, SST, ETSS, NTSS, PR, and SSR data were acquired from the fifth-generation ECMWF reanalysis for the global climate and weather (ERA5, Hersbach et al., 2020). The surface CHL is from NEMO-PISCES. All are monthly averaged data on single levels at 0.25° resolution.

For pre-processing, we standardized the resolution of all 0.25°×0.25° data to 1°×1° by consistently calculating the mean within each 2×2 grid. We selected a total of 312 months from January 1993 to December 2018 as the training set, and 24 months from January 2019 to December 2020 as the testing set for testing the temporal extrapolation capability of the network. During training, to prevent overfitting of the model, we implemented the early-stopping technique (Prechelt, 2012) and selected 24 months from our training set (312 months) as a validation subset. The selection of the training validation and training sets was random, with a fixed random seed to ensure reproducibility. Before inputting the variables into the networks, all missing values in the variables were replaced by 0 to ensure the completeness of data after applying z-score normalization to them.

To better examine the performance of network prediction, as well as the PISCES model, GLODAPv2.2023 was adopted. It includes in situ data from 724 cruises conducted by various international research projects, among which 530 received successful quality control (A. Olsen et al., 2016). After filtering these data based on our research scope in terms of depth (0-680 m depth), region (30°S-30°N, 30°E-120°E), and years (1993-2020), a total of 22,184 nitrate measurements were selected to be utilized in Section 4.

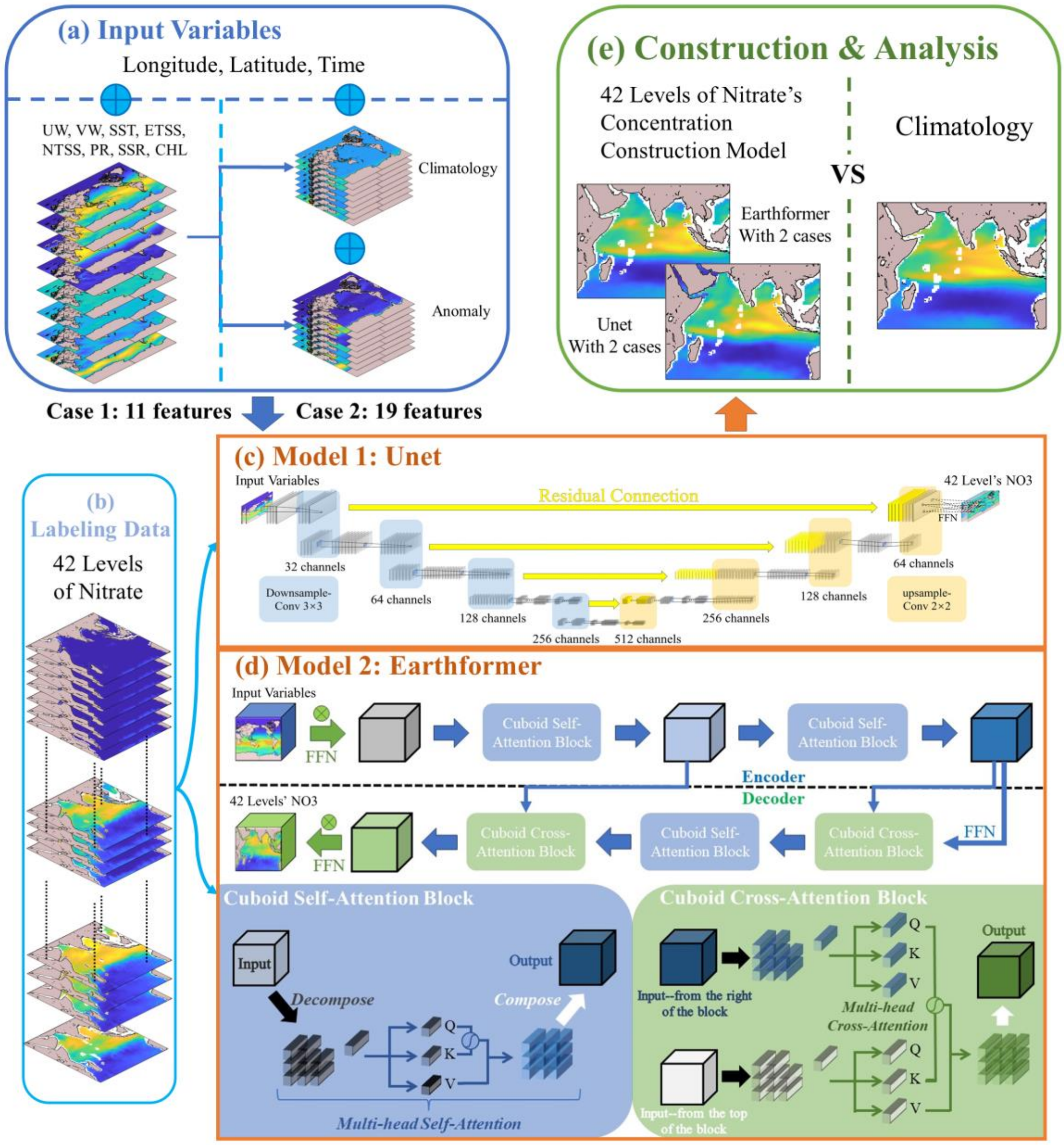

Figure 2. Flowchart for the reconstruction of nitrate levels in the Indian Ocean based on U-net and Earthformer respectively.

2.2 U-net

As shown in Figure 2(c), U-net consists of an encoder and a decoder that form a U-shaped diagram. The encoder down-samples the input features while increasing the number of channels in the hidden information, compressing complex information from input features (e.g., sea surface temperature field and wind field as shown in Figure 2(a) and reducing the spatial dimension of the fields. Pre-experiment showed that deepening the down-sampling processes can slightly improve (for <5%) our reconstructions but cause much more computational consumption. Therefore, in our implementation, the encoder consists of five down-sampling layers, each including two 3x3 convolution layers, two batch norm layers, and a 3x3 with 2 strides convolution layer for down-sampling, yielding 32, 64, 128, 256, and 512 hidden features. Through each layer, the spatial dimension was reduced by a factor of 2. Each hidden feature can be treated as a spatial map that includes abstract deep information. The decoder restores the resolution of the fields using bilinear interpolation, it consists of four up-sampling layers containing an interpolation function, followed by two 3x3 convolution layers, two dropout layers (with a rate of 40%), and two nonlinear activation layers, to sequentially generate 256, 128, 64, and 32 hidden features back. Residual connections link the encoder and the decoder as a 'bridge', to help the decoder utilize the information of compressed feature fields from the encoder, enabling better capture of higher-level processed features. Finally, the final output layer (FFN in Figure 2c) adjusts output channels through a linear layer to produce 42 levels nitrate. More rationale and interpretation of U-net can be found in X. Li et al. (2020).

2.3 Earthformer

Earthformer is a deep-learning neural network based on Attention and Cuboid decomposition. Given that we have applied this network in our recent work (Liu et al., 2024), only brief information on this network is provided here. Readers are referred to the network architecture in Liu et al. (2024) The structure of Earthformer used in our research is depicted in Figure 2(d).

For our input feature fields, which are high-dimensional, nonlinear, and non-uniform, it is challenging to analyze each feature. Therefore, selecting relevant key points in the input features as the most important and representative parts is needed, to obtain the most valuable information for nitrate prediction. This is the core idea of the Attention mechanism, which can be considered as a trainable weight mask that gives large weights to the more important grid points. To reduce the computation burden, Cuboid Attention is a modified version of Attention. It first decomposes our feature fields into smaller feature cuboids using different types of decomposition, such as dividing them based on longitude or latitude. Then, Attention is applied to extract key elements for predicting nitrate. Earthformer also has a similar encoder-decoder structure to U-net. Cuboid self-attention refers to applying Cuboid Attention to the information passed within the encoder or decoder. Cuboid cross-attention, on the other hand, only happens in the decoder, applying Cuboid Attention to the combination of information passed from the encoder and the information from the decoder itself. After passing through these blocks in the encoder-decoder, a final FFN layer is applied to adjust the output channels, resulting in 42 levels of nitrate.

2.4 Experiment design

To test the sensitivity of different network and input data schemes, we design experiments as presented in Table S1 in Supplementary Material. The input has 11 features in Case 1. For Case 2, the input features are preprocessed by removing the climatology component from 1993 to 2018. The anomaly component of the original features and climatology components are combined as the new 19 input features. The input data have global coverage, but we only utilize data from the Indian Ocean region to calculate the loss. Pre-experiments that incorporating time lag did not improve the reconstruction, so we only used the inputs of the same month with the nitrate in the reconstruction. For each experiment, we stop training when either a maximum iteration of 1200 is reached, or no improvement is observed for the validation subset for 120 consecutive iterations.

2.5 Statistical metric

We use the normalized root-mean-square error (*NRMSE*) to quantify the reconstruction error. NRMSE was proposed to avoid the scale dependency (Shcherbakov et al., 2013). In our research, RMSE is calculated between the given predicted values and the corresponding labeling values, while NRMSE is RMSE divided by the mean of the corresponding labeling values. Similar calculation of NRMSE has previously been applied to evaluate the reconstruction performance of neural networks for surface chlorophyll time series (Martinez et al., 2020). It is important to note that NRMSE serves as a relative measure, and does not possess significant numerical meaning on its own. But it enables effective comparisons of network performance across various depths or regions.

Moreover, to facilitate the comparison of the four-dimensional spatiotemporal field of nitrate, we define two new metrics, namely the relative climatology superiority vertical spatial ratio (*RCVSR*) and the relative climatology superiority horizontal spatial ratio (*RCHSR)*. Both indexes compare the network prediction with the climatology prediction, i.e., use the climatological value as the 'prediction', given that the nitrate concentration in the ocean interior largely follows the climatological values.

Once network results and the climatology values are given, *RCVSR* is a function of x and y. The *RCVSR* is the proportion of months in which neural network prediction outperforms climatology prediction. This comparison is based on a statistical metric (here, NRMSE) used to evaluate the performance of reconstruction for a specific month. If the metric shows that the network is better than the climatology prediction in that month, that month would be recorded and contribute to the calculation of the overall proportion within the comparison time interval. Similarly, *RCHSR* is a function of time. The *RCHSR* at that time t is the proportion of levels where a neural network outperforms (also using NRMSE) climatology prediction, calculated across all levels.

2.6 Interpretability analysis

To better explain the prediction of the neural network, the Integrated Gradients (IG) method was adopted from Sundararajan, Taly, and Yan (2017), which has been used to assess the sensitivity of a mixed layer depth prediction network (Foster, Gagne II, & Whitt, 2021) and analyze the activation in the last convolutional layer of an SST prediction model

(Feng et al., 2022). The IG sensitivity $S_{i,j,k}$ can be represented by the following formula:

$$S_{i,j,k} = (x - x_{baseline}) \int_{\alpha=0}^{1} \frac{df(\alpha x - (1-\alpha)x_{baseline}))}{dx_{i,j,k}} d\alpha$$

In our study, f represents the network prediction, and $X^{(H,W,K)}$ represents a batch (month) of our normalized input, with H and W are the spatial grid points of the input field, and K as the number of features (11 or 19 in total). Subscript i, j, k belongs to H, W, and K, respectively. In the equation, $\frac{df(.)}{dx}$ refers to the gradient with respect to a particular input. We set $x_{baseline} = 0$. Then the equation can be re-written as:

$$S_{i,j,k} = x \int_{\alpha=0}^{1} \frac{df(\alpha x)}{dx_{i,j,k}} d\alpha$$

The $S_{i,j,k}$ refers to the integration of gradients across all the layers of the network and can be calculated using the chain rule.

For the nitrate at a specific location $(x_{t,}y_{t,}z_t, t)$, $S_{i,j,k}$ measures the contributing strength of every input feature, each as a two-dimensional map. To better visualize such a high-dimensional matrix as a function of $(x, y, k, x_t, y_t, z_t, t)$, a target region $(x_{t,}y_{t,}z_t)$ must be chosen. We choose the upper 100 m of the adjacent Java area as the target region and integrate all $S_{i,j,k}$ within. This integrated quantity will be represented by ω, which is one two-dimensional feature importance map for each feature in each month. Statistically, ω can be an analog to the slope of multivariate linear regression, which will be shown in

Section 3.4.

3. Results

3.1 Spatial Comparison

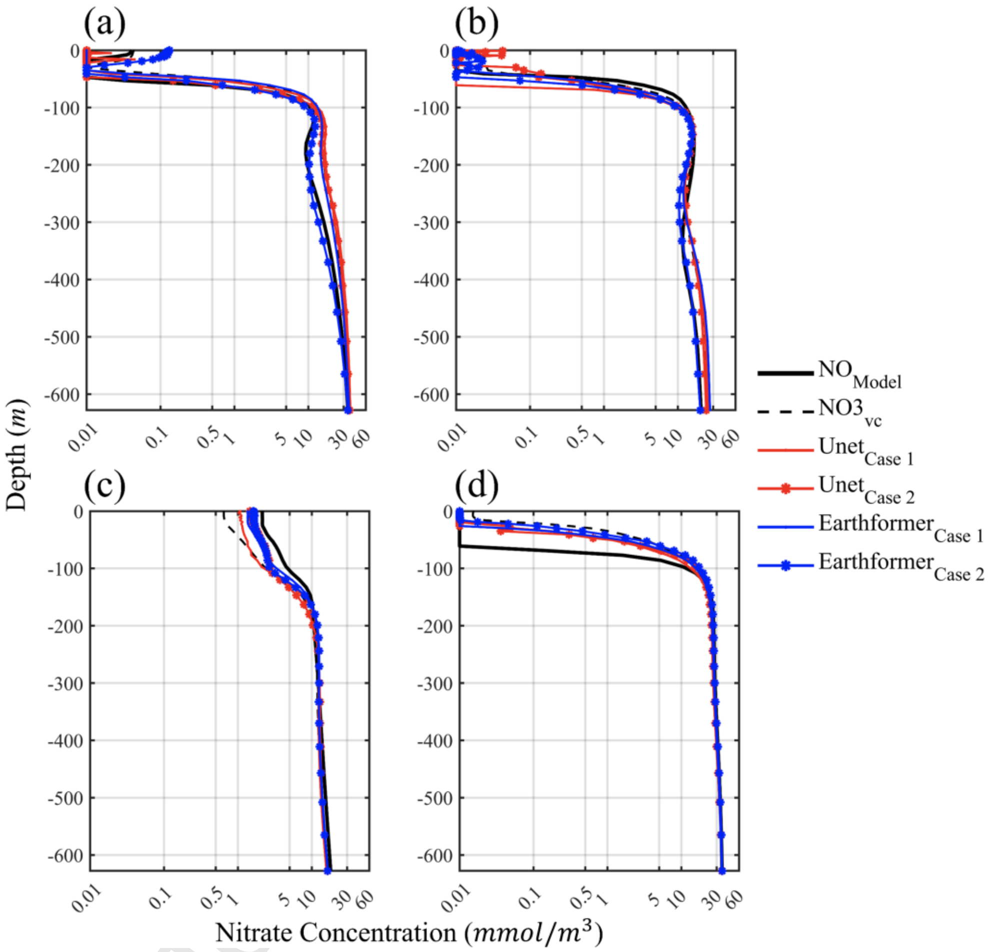

Figure 3. Vertical distribution of nitrate concentration at selected sites (see Figure 1 for their locations) for December 2019. (a) Bay of Bengal, (b) Arabian Sea, (c) South Indian Ocean, and (d) Central Basin. The x-axis is at a logged scale.

Using December 2019 as an example, we selected eight representative locations to check the vertical profiles of nitrate (in Figure **3**). Significant biases are observed in the near surface predictions, especially in the central basin (Figure **3**d), where the predictions even failed to accurately predict the mixed layer depth, overestimating it by approximately 30m compared to the model value; but under the 100m, the difference between the BGC model and the reconstruction (also the climatology prediction) is relatively smaller, implying a dynamic source for such discrepancy, instead of a biology source, since most of the biological activities influencing nitrate occur near surface. At two sites located in marginal seas (Figure **3**a-b), U-net also fails to predict the subsurface nitrate structure of this month, with the reconstructed profile close to the climatology prediction, the overestimation of nitrate reaches its maximum at ~200m (nearly 10 mmol m^{-3}, i.e., ~100 % deviation); The Earthformer largely corrects this bias, with its vertical distribution close to the model in the subsurface area. Results of all methods have clear deviation in the upper 50m, which is related to the strong biological processes occurring in the surface layer that affect nitrogen cycling.

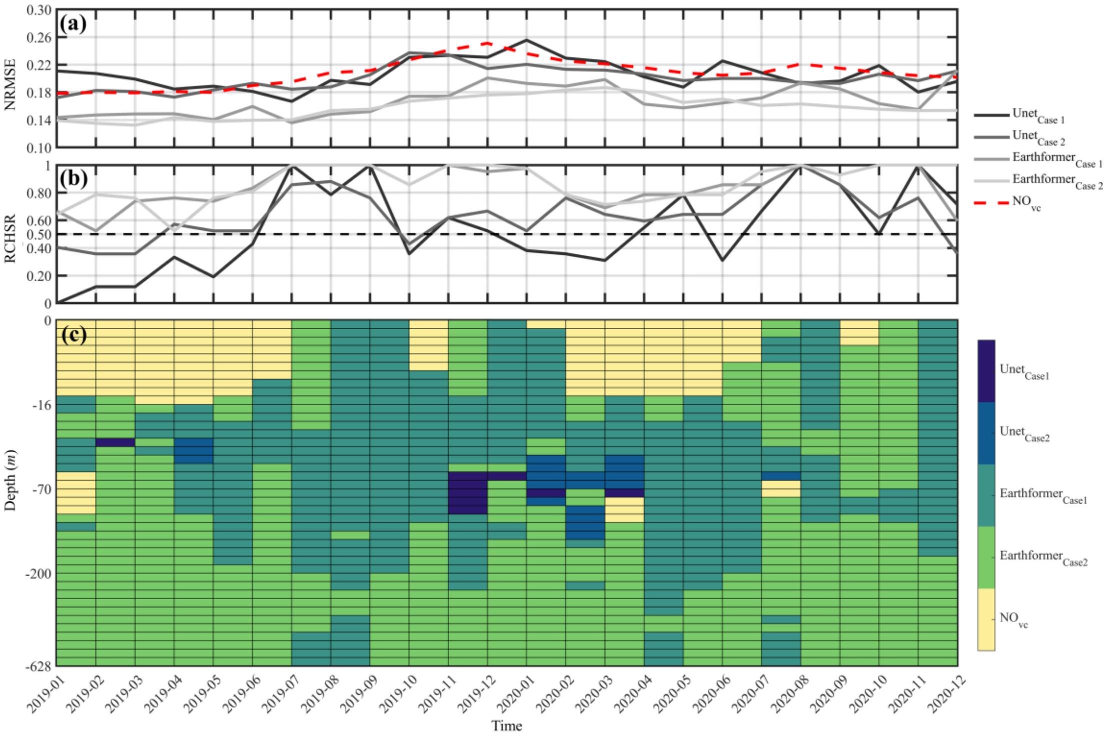

Figure 4. (a) Spatial NRMSE for each month (b) *RCHSR* summarizing spatial NRMSE from Jan 2019 to Dec 2020 for U-net Case 1, U-net Case 2, Earthformer Case 1, and Earthformer Case 2. (c) Time-depth distribution of the optimal method based on the *RCHSR* calculation process. Each grid represents the method with the minimum horizontal NRMSE at that month and that level.

In Figure 4(a), we can observe that regardless of the month, all reconstruction results exhibit an NRMSE below 0.3 in spatial distribution, higher in Dec, Jan, and Feb. Among them, U-net and the climatology prediction show similar performance, with a maximum NRMSE of ~0.26 in January 2020, indicates 26% error with respect to the monthly average nitrate in this month. On the other hand, Earthformer stands out with consistently lower NRMSE below 0.2, generally better than all other methods, while the difference in the input features (Case 1 vs Case 2) is small. We presented one of our new-defined metrics, *RCHSR* in Figure 4(b), for a more thorough statistical comparison of the spatial performance of AI networks and the climatology prediction. The Earthformer consistently achieves *RCHSR* > 0.5, i.e., more than half of the levels perform better in the horizontal dimension. From January to June 2019 and from December 2019 to March 2020, the *RCHSR* of U-net Case 1 consistently remains lower than that of U-net Case 2. U-net Case 1 even has *RCHSR* = 0 in January 2019. This reinforces the finding that the methods using U-net did not outperform the climatology prediction in most cases, suggesting the inadequacy of CNNbased networks for the complex nitrate reconstruction task.

We also examined the time-depth distribution of the performance (Figure 4c). It is evident that although the network methods, especially Earthformer, outperform the climatology prediction significantly in the *RCHSR* comparison (Figure 4b), their ability to predict nitrate in the top 15 levels (about 0-16m depth) is notably weaker. Specifically, from Jan through Jun, the climatology prediction emerges as the optimal method for nitrate prediction in the top levels. In other months or layers, networks still demonstrate their advantage, among them, Earthformer consistently outperforms U-net.

3.2 Temporal Comparison

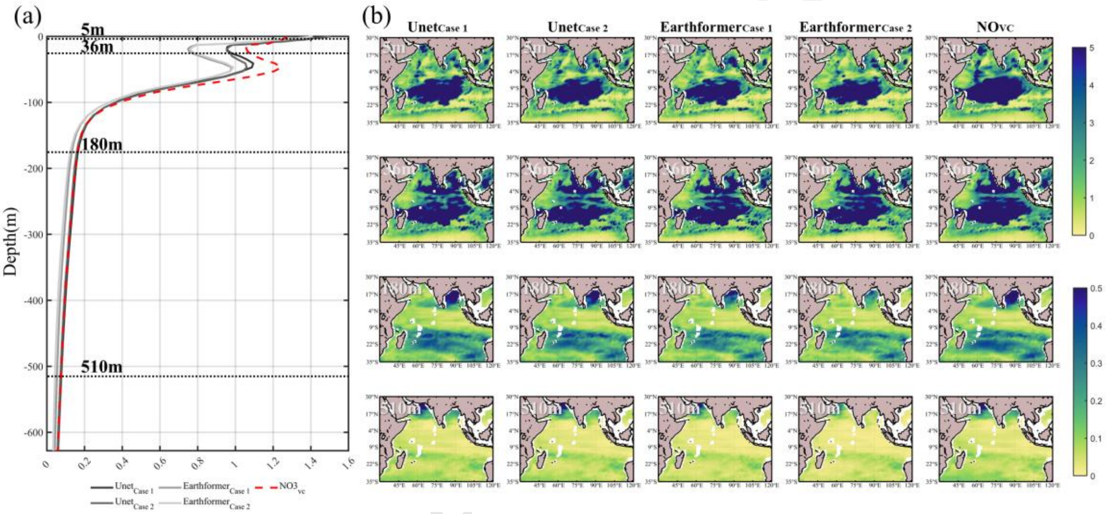

Figure 5. (a) Temporal NRMSE for each layer. Horizontal dotted lines represent the corresponding depths (5 m, 36 m, 180 m, and 510 m) for each row of subplots at the right side. (b) Horizontal distribution of Temporal NRMSE at the depths of 5 m, 36 m, 180 m, and 510 m based on the reconstruction results over 24 months in the testing set.

In Figure 5a and b, all methods perform poorly at the surface in temporal reconstruction, especially in the central basin region, which is consistent with the trend shown in Figure **3**. For 50m and deeper, the NRMSE of all methods gradually decreases, and the reconstruction results in different regions are better compared to the surface. For the upper 100m, the NRMSE is >0.4 (Figure 5a), meaning a more than 40% error with respect to the horizontal-temporal average nitrate in corresponding level. Earthformer Case 2 has systematically low NRMSE for ~0.3 relative to climatology prediction, which is a significant improvement. In Figure 5b, although the reconstruction performance is better in the deeper layers compared to the upper layers, there are significant regional differences. The NRMSE at 180m in the Bay of Bengal and at 510m in the nearshore areas of the Arabian Sea are notably higher than other regions, with maximum values exceeding 0.5. In contrast, the reconstruction performance in most regions at 510m does not exceed 10%, as the NRMSE in these areas is less than 0.1. These general performance patterns or differences can be explained by environmental controls.

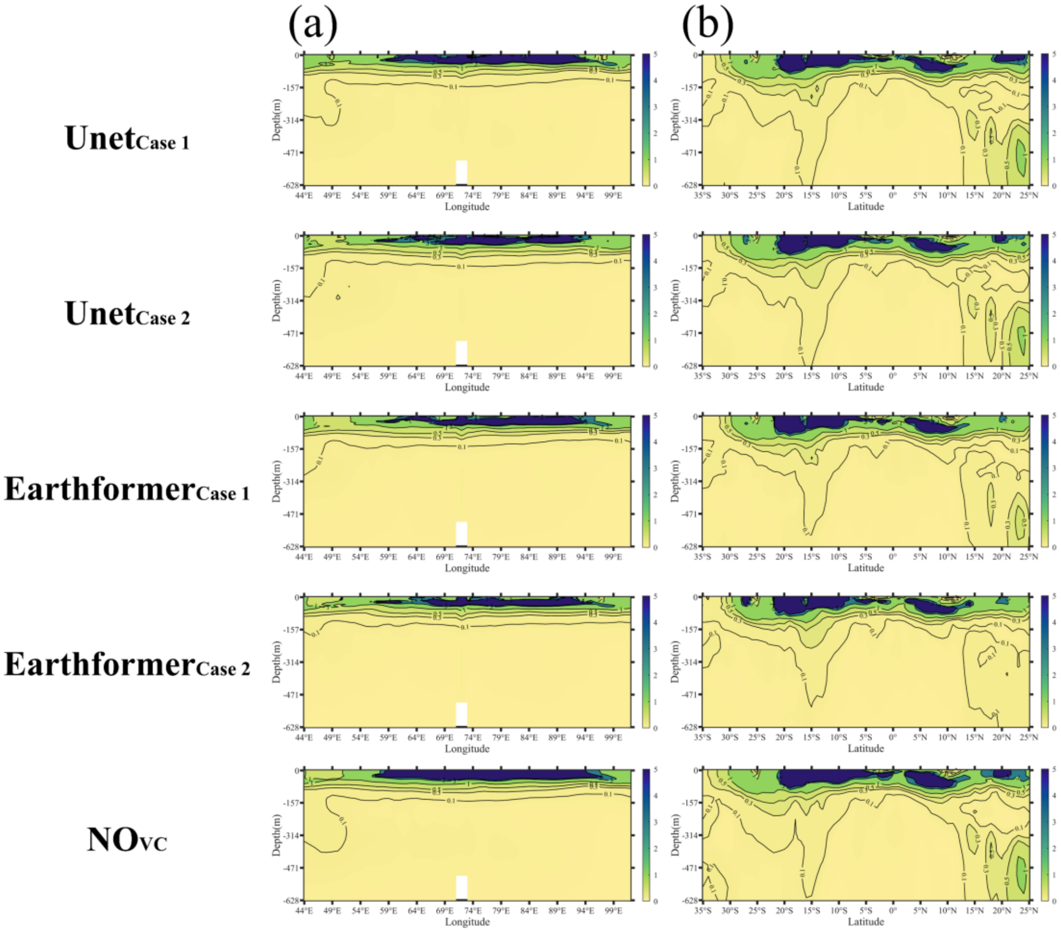

Figure 6. Vertical distribution of temporal NRMSE along (a) Transection A and (b) Transection B (see Figure 1 for their locations) derived from different reconstruction results of methods. The blank areas present in the subplots are due to data gaps caused by topographical reasons.

To provide a more comprehensive assessment of the performance of each method, two sections were chosen, i.e., meridional Transection A (at 7°S) and zonal Transection B (at 64°E), to analyze the basin-scale reconstruction in different networks. In the zonal direction (Figure 6a), all methods demonstrate strong temporal reconstruction capability under approximately 150 meters, with NRMSE values below 0.1, indicating errors regarding the 2019-2020 temporal average model values in corresponding grids less than 10%, consistent with the vertical profile of NRMSE in Figure 5. Both U-net and the climatology approach exhibit similar NRMSE values and show lower performance compared to Earthformer in the western Indian Ocean. In the meridional direction (Figure 6b), notable differences are observed in the performance of all methods. Earthformer exhibits the lowest NRMSE, followed by U-net, both outperforming the climatology prediction. Generally, Case 2 for each network outperforms its corresponding Case 1, with lower NRMSE values observed in the Northern Indian Ocean. It is important to highlight that all methods exhibit poor temporal reconstruction performance in the near-surface ocean (<150m), particularly in the central basin and the Northern Indian Ocean (from 20°S to 3°S and from 59°E to 94°E), where NRMSE in most of these grids exceed 5. For the central basin, the existence of subtropical gyre and relatively low biogeochemical activities lead to high reconstruction uncertainties therein. For the water column in the Arabian Sea or 15°S (Figure 6b), the poor performance can even penetrate down to 600 m. This could be attributed to the complex biogeochemical processes in these regions, such as the wind-driven upwelling. Indeed, the water with lower performance collocates with the upwelling-driven high productivity, subsequent carbon export (F. Li et al., 2023), and remineralization (in the deep layer) in the Arabian Sea (Sarma, Bhaskar, Kumar, & Chakraborty, 2020). Interestingly, the deep equatorial Indian Ocean seems to perform better, which is dominated by slow physical nutrient transports so that persistent to changes. These slow physical dynamics can be better predicted by surface dynamic factors such as SST or SSH.

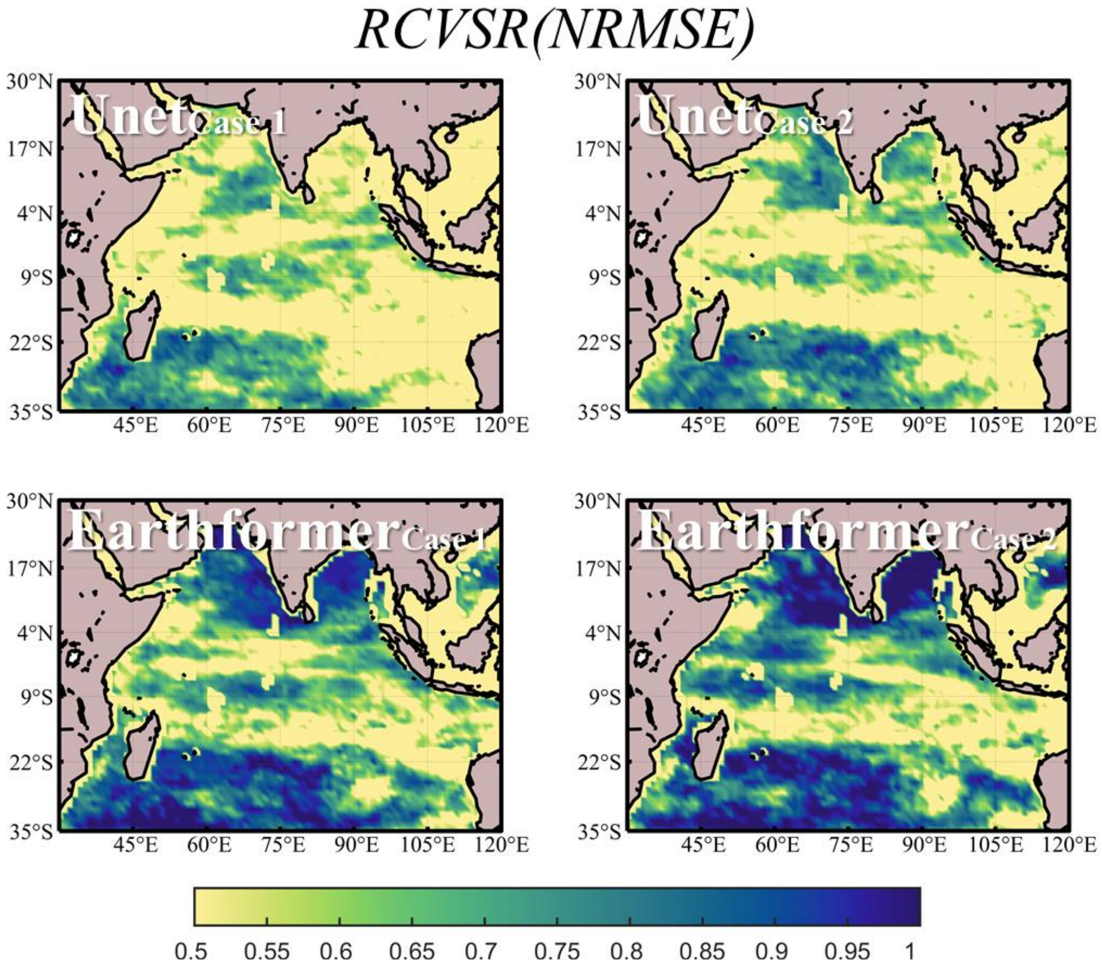

Figure 7. *RCVSR* summarizing temporal NRMSE among different levels for U-net and Earthformer in Case 1 and Case 2 respectively. The regions with RCVSR < 0.5 are shown in yellow.

When looking into the pattern of *RCVSR* based on NRMSE (Figure 7), both U-net and Earthformer methods show similarity. In the nearshore region of the northern Indian Ocean or in the southern Indian Ocean, Earthformer achieves the highest *RCVSR* at ~0.9, indicating more than 90% vertical levels in these regions perform better than their corresponding climatological value, compared to that of U-net at ~0.7. The networks have large *RCVSR* regions exceeding 0.5, these regions are located in the northern and southern areas of the Indian Ocean, with Earthformer averaging around 0.9 and only a few areas above 0.9 in U-net.

3.3 Overall Comparison

By calculating their overall NRMSE, it is evident that Earthformer Case 2 achieves the best performance with a value of 0.1591 (Table **1**), meaning 16% error in terms of overall average nitrate, surpassing all other methods. The performance of U-net is comparable to that of the climatology prediction. Consistent with the previous discussion, all methods exhibit larger errors in the surface layer. Among the two different neural network architectures, Case 2 consistently outperforms Case 1, indicating that the decomposition of input features improves the reconstruction capability of the models.

Table 1. The overall, pattern, and profile NRMSE of different methods. Only the maximum and minimum values are shown in pattern metric and profile metric, along with the corresponding depths or time points. Each value of the pattern NRMSE was calculated from the 3D nitrate field of (x, y, t) and is a function of depth. Profile NRMSE is from 3D nitrate field of (x, y, z) and is a function of time.

Methods	Overall NRMSE	Pattern NRMSE		Profile NRMSE	
		Maximum	Minimum	Maximum	Minimum
U-net Case 1	0.2068	1.4985(1m-level)	0.0596(628m-level)	0.2555(2020.01)	0.1668(2019.07)
U-net Case 2	0.2007	1.5029(1m-level)	0.0565(628m-level)	0.2372(2019.10)	0.1722(2019.01)
Earthformer Case 1	0.1688	1.4067(1m-level)	0.0424(628m-level)	0.2116(2020.12)	0.1359(2019.07)
Earthformer Case 2	**0.1591**	1.4099(1m-level)	0.0338(628m-level)	0.1868(2020.03)	0.1325(2019.03)
Climatology	0.2089	1.2727(2m-level)	0.0586(628m-level)	0.2510(2019.12)	0.1785(2019.01)

We then choose the adjacent Java Sea (AJS) as the zoom-in area to further look into the nitrate reconstruction, and focus on the interannual variabilities. Here we define the AJS as 98°E-117°E and 12°S-3°S. During El Niño years, specifically in 2011, 2015, and 2019, anomalous increased nitrate concentration was observed therein (Wahyudi et al., 2023). Following their study, we compare the climatology with the reconstructed nitrate in 2019 to assess the discrepancies.

Driven by the strong El Niño and Indian Ocean Dipole events, the year 2019 was significantly abnormal in terms of biogeochemistry. As shown in Figure 8(a), the nitrate concentration was significantly positive > 0.8 mmol m^{-3}, much larger than the climatology values of ~0.2 in October. We present Figure S1 (Supplementary Material) to compare near-surface (5 m) nitrate concentration variations in the AJS. The western AJS exhibited a nitrate anomaly, peaking in October 2019, consistent with the study of Wahyudi et al. (2023). The high nitrate concentration appeared to be coastally trapped and gradually decreased away from the coastline. In terms of temporal variation, the elevated nitrate concentration could be observed early in June, where nitrate concentration near 117°E in June 2019 was significantly higher compared to that of June 2020, and this phenomenon is well reflected by the reconstruction of Earthformer Case 2. In contrast, the climatology has limited capability in capturing these anomalies.

In terms of driving factors (Figure 8b) for such anomalies, variables such as PR, CHL, SST, and SSR all exhibited considerable anomalies this year. Specifically, CHL and SSR were higher than the values in the same period of 2020, while SST and PR were lower. This indicates that the network successfully captured these anomalies and performed the reconstruction of nitrate on a physical basis.

Surprisingly, the wind speed and wind stress, which are the main drivers of upwelling in this region (Susanto, Gordon, & Zheng, 2001), did not exhibit significant differences between the two years, despite being influenced by positive ENSO and IOD events that resulted in the strengthening of southeast winds in the eastern Indian Ocean. This can be explained by the fact that the monsoon effects in the tropical Indian Ocean tended to be remote forcing, especially interannually, driving the AJS in the form of Kelvin waves (Chen, Han, Li, & Wang, 2016), instead of direct forcing.

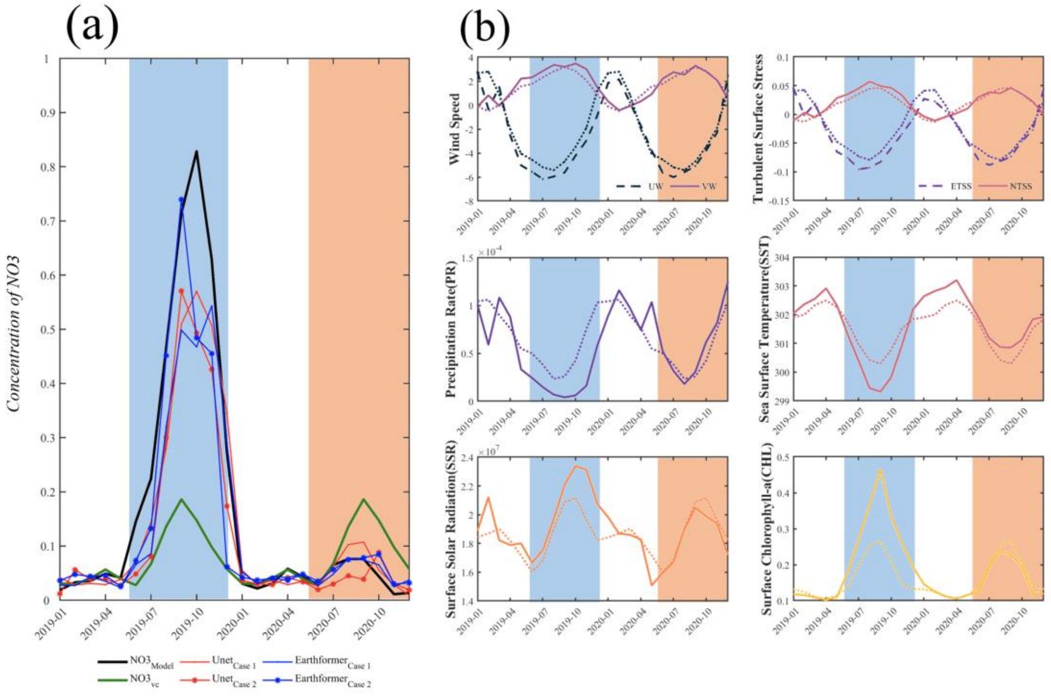

Figure 8. The near-surface (5 m) nitrate concentration and its driving factors averaged in

the AJS. (a) Nitrate in 2019-2020, with the model value of nitrate (black lines) and its climatology (green lines), results of U-net Case 1 (red lines), U-net Case 2 (red lines with asterisks), Earthformer Case 1 (blue lines) and Earthformer Case 2 (blue lines with asterisks). (b) Driving factors in 2019-2020. In each subplot, the solid line represents one or two input features corresponding to the subplot and the dashed line represents its climatology. Both in (a) and (b), the blue and orange shadings highlight the periods of further investigation.

3.4 Network interpretation

To better understand the reconstruction of black-box neural networks, we use the IG method to compute the feature sensitivity in the best-performance case, Earthformer Case 2. As depicted in the time series in Figure 9(a), the seasonal variation of the domain-averaged sensitivity ω is much stronger than its interannual variabilities, indicating the nitrate in AJS is dominant by seasonal variation of wind, with secondary influences from the interannual variation (e.g., ENSO or IOD). The ω time series of various features exhibits seasonal contrasts between the DJF and JJA, meriting further investigation. Note that JJA is chosen to investigate the precursor of the Oct peak. In Figure 9(d-f), most features show higher ω during DJF compared to JJA, while PR is the opposite. The CHL contribution reflects the influence of biogeochemical factors, but its contribution seems unexpectedly low, in turn implying the importance of physical factors. Among physical factors, the SST and SSR appear to be weakly contributing, while the wind and its stress tend to be more important, suggesting the dominant role of dynamic factors outcompeting thermal factors in regulating nitrate. Among all factors, UW, VW, and PR have the largest ω and exhibit the most pronounced seasonal variations, we focus on these features to investigate the underlying reasons for these seasonal variations in the subsequent analysis.

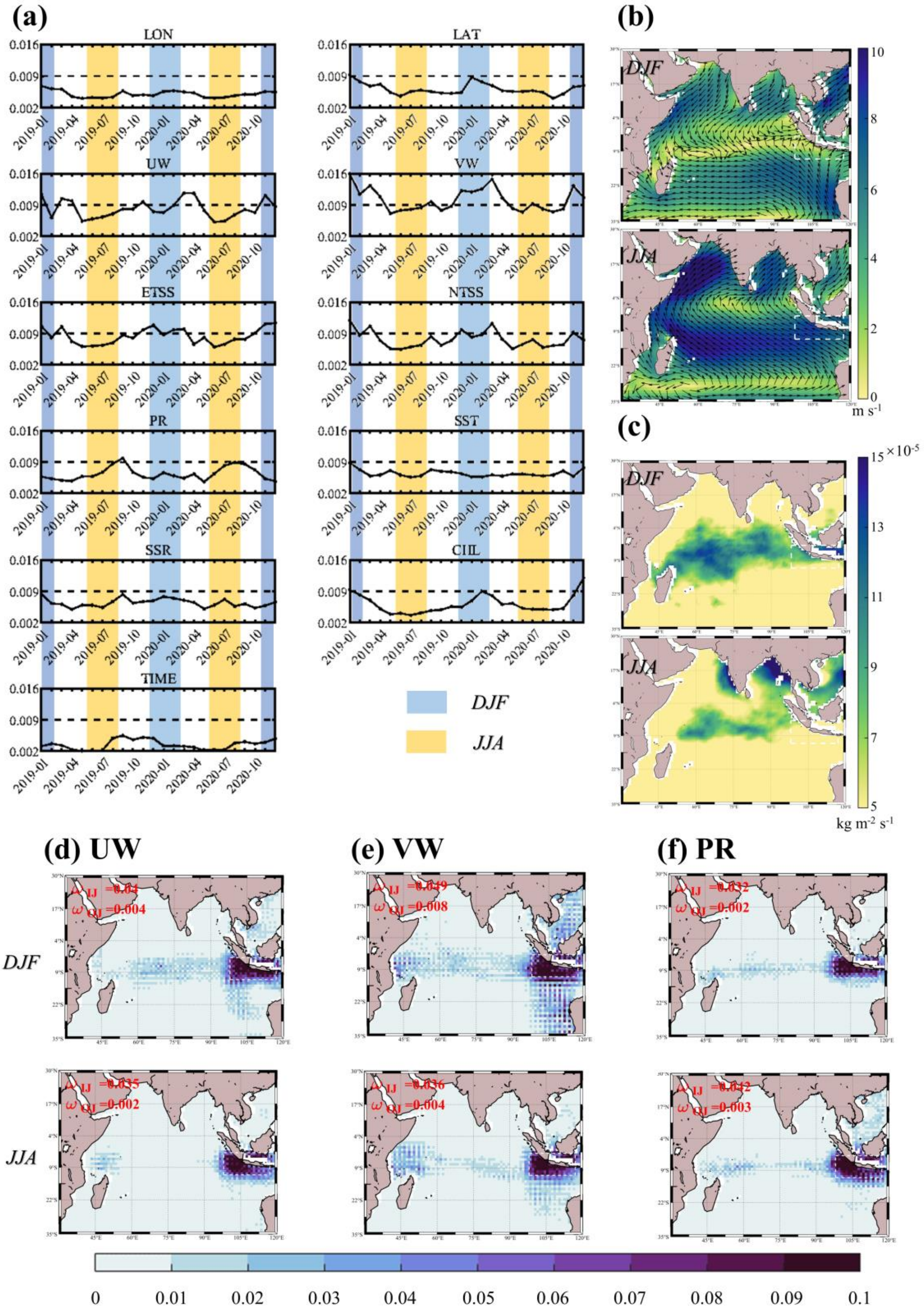

Figure 9. Feature contribution to nitrate in the AJS in Earthformer Case 2. (a) The temporal variation of the spatial-average ω over the whole domain of each input feature. The blue shading represents DJF (Dec-Jan-Feb), while the yellow shading represents JJA (Jun-Jul-Aug). (b) Wind direction (vectors) and wind speed (color shading, in m・s^{-1}) in

DJF and JJA. (c) PR in DJF and JJA (in kg・m^{-2}・s^{-1}). (d-f) Feature contribution (ω) for UW, VW, and PR in DJF and JJA. In each panel, ω_{IJ} represents the AJS-average value, while ω_{OJ} means the average outside the AJS. The white dashed box delineates the area of the AJS.

Interestingly, the most important three factors (UW, VW, and PR) present distinct seasonal differences in feature contributions (Figure 9d-f). Within the AJS, the wind has a higher impact on AJS nitrate in DJF than in JJA, while PR has less impact. Outside the AJS, the opposite is true, as higher wind impacts in JJA and lower PR impacts in DJF. The feature contribution appears to be more scattered for the DJF wind, particularly with meridional linkage to the South China Sea and Australian coasts. This pattern is strongly contrasted with that in JJA, in which only small portions outside AJS have impacts and the impacts have remote impacts from the western tropical Indian Ocean.

These seasonal contrasts can be explained with corresponding wind and PR patterns (Figure 9b-c). In JJA, the winds exhibit a homogenous basin-wide clockwise pattern, with southeastern winds covering the AJS and broader Southern Indian Ocean. On the other hand, during DJF, the wind distribution is more chaotic, with the wind speed being especially weak over the AJS. In the case of DJF, limited information from the wind would be required for the network to generate nitrate responses, while chaotic forcing generates a more sensitive response in the network. This reflects the Earthformer network based on attention that can extract important spatial information automatically, paying more weight to these important locations. Dynamically, these differences between JJA and DJF are in line with the seasonal variations in the Walker circulation and Hadley circulation (Schwendike et al., 2015). In JJA, the tropical wind can also trigger ocean circulation jet and Kelvin waves (Wyrtki, 1973) to remotely influence AJS.

The above interpretation also can apply to the opposite patterns observed in PR. As shown in Figure 9(c), PR during DJF exhibits a more regular pattern with the only hotspot in the tropics. During JJA, there is minimal rainfall in the south Indian Ocean, while there are several regional high PR hotspots in the Arabian Sea, the Bay of Bengal, and the South China Sea. Therefore, in JJA, the network requires more information to reflect the impact of PR on nitrate concentration, leading to a scatter importance map. In contrast with the wind, the PR effects tend to be local effects, with the exception of the cross-basin influence from the South China Sea in JJA. Dynamically, this might reflect the negative correlation between weak PR in AJS and strong PR in the South China Sea, which is due to water and heat exports from tropical AJS to the South China Sea (Xu et al., 2021) during JJA. Specifically, the Australian Southeast Monsoon brings cool and dry air currents reducing rainfall in AJS (Siswanto & Suratno, 2008). In contrast, at the same time in the South China Sea (SCS), the Southwest Monsoon from the eastern Indian Ocean transports heat and water, leading to increased rainfall in the SCS.

4. Discussion

Reconstruction of gridded nitrate data presents a significant challenge due to the inherent difficulty in obtaining large scale nutrient data. Satellite observations lack sensors that can directly sense nutrient concentrations. While indirect estimation of surface ocean nitrate (Arteaga et al., 2015) has achieved high precision using a series of sea surface remote sensing data, it lacks the capability to reconstruct the ocean interior (Klemas & Yan, 2014). Direct observation with Biogeochemical-Argo or other automatic platform (Chai et al., 2020) could provide inexpensive and timely 3D nutrient observations, but their numbers for now are far from enough to achieve global and near-real-time coverage. Therefore, currently using AI to indirectly reconstruct nutrient structure, particularly from full-coverage surface data, is a promising way. However, such reconstructing the 3D structure of ocean nitrate is a more complicated task as it requires consideration of various physical and biogeochemical factors. Cautions should also be taken in choosing the training data, since the model data used here is merely a simplified representation of the real ocean that could be more complex and noisy (Tagliabue, 2023). At least, with carefully designed such data-driven methods, the reconstructed results only showed little difference from the PISCES when compared to the observation data. This indicated that data-driven reconstruction based on model data would be not significantly affected by error propagation resulting from discrepancies between the model data and the observation.

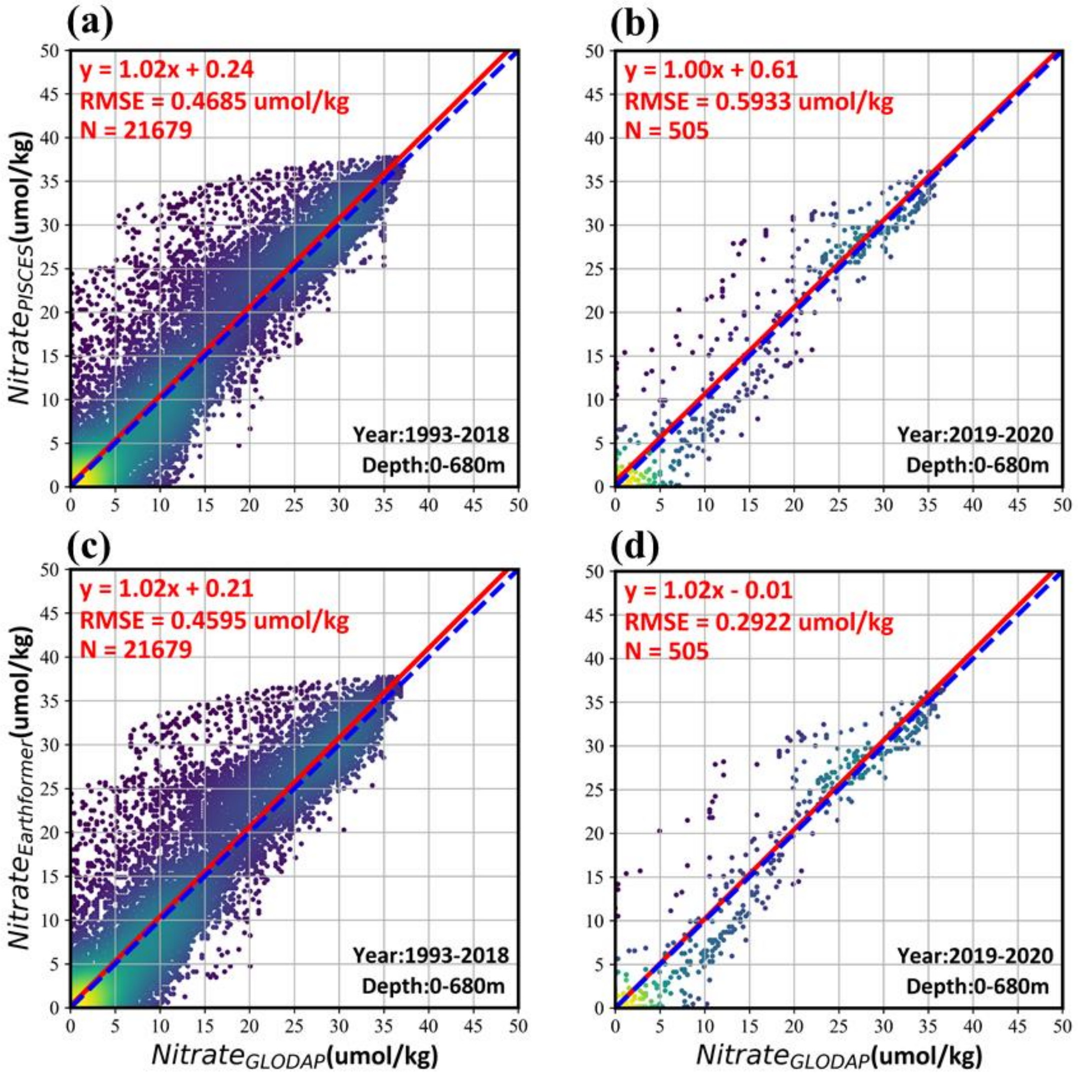

Figure 10. Density plot and fitted curve comparing nitrate concentrations between PISCES model and GLODAP in situ measurements among 1993-2018 (a) and 2019-2020(b), similarly, between Earthformer Case 2 and GLODAP in situ measurements among 1993-2018 (c) and 2019-2020(d). In situ data from GLODAP has been matched with gridded monthly data from PISCES or the network reconstruction.

On the other hand, deep learning methods are generally considered black-box (Fan, Xiong, Li, & Wang, 2021; Holm, 2019; Portillo Juan, Matutano, & Negro Valdecantos, 2023) inhibits their further applications (Reichstein et al., 2019). Despite their usefulness in various environmental tasks including oceanic reconstruction (Konya & Nematzadeh, 2024), critiques of lacking network interpretability often limited the further generalization of these data-driven models. To tackle this issue, network interpretation is a feasible strategy that possesses fundamental importance (Ham, Kim, & Luo, 2019; Park et al., 2022; Samek, Montavon, Lapuschkin, Anders, & Müller, 2021). In our study, we attempted to understand the neural network prediction using the IG method. We argue this method is universal that can be further applied to many problems in oceanic, environmental, and climate sciences.

Moreover, to tackle the interpretability issue of AI models, we can also consider physics-constrains. This is an emerging paradigm that is expected to further improve data-driven forecasting, by incorporating the advantages of numerical models and data-driven forecasting tools while simultaneously avoiding the disadvantages of either methods (Dong et al., 2022; Karniadakis et al., 2021). There exist methods that can incorporate ecological processes into AI, such as the Physics-Informed Neural Networks (Raissi, Perdikaris, & Karniadakis, 2019), and can enable AI to learn complex ecological processes (Holder & Gnanadesikan, 2021; Lek & Guégan, 1999).

5. Conclusions

In this study, two AI networks, U-net and Earthformer, were applied to prove the availability of reconstructing the 3D structure of nitrate concentration in the Indian Ocean only from surface data (UW, VW, ETSS, NTSS, PR, SST, SSR, CHL) and spatiotemporal information (LON, LAT, TIME). As a first step of concept proofing, we adopted a physical-biological model forced by climate reanalysis (ERA5) as the input, training, and testing sets. The results show that the Earthformer can outperform the U-net network, with the input features decomposed into climatology components and anomaly components. The Earthformer exhibits superior reconstruction with the lowest overall NRMSE (0.1591), surpassing the performance of U-net and climatology prediction. Further comparison with observed profiles suggests that our nutrient reconstruction, trained from PISCES, reaches a lower RMSE (0.2922 umol/kg) in 2019-2020, and performs comparably or even better than PISCES itself (0.5933 umol/kg).

We used the AJS region to see if the network could capture the interannual variation of nitrate. Indeed, the nitrate structure in AJS in Oct 2019 presented an anomalous high, which was well captured by the Earthformer reconstruction. We further applied a deep learning interpretation technique named the Integrated Gradients (IG) to compute the spatio-temporal contribution/importance of every input feature to upper-layer nitrate in the AJS. The seasonal variations of wind and precipitation contribution presented distinct contrasts. These distinctions can be explained by the understanding of dynamic controls on the ecosystem.

Reconstructing gridded nitrate data is a significant challenge as satellite observations cannot directly sense nutrient concentrations, on the other hand, existing indirect estimation methods are unable to capture the internal structure of the ocean. Unlike previous studies using 3D temperature and salinity as the input, our proof-of-concept study utilizes only surface information, and highlights the potential to reconstruct long-term and large-scale nitrate (as well as other ecosystem variables) structures with AI. For example, these methods can be applied to reconstruct the historical nitrate structure to study the impacts of marine heat waves (Zhan, Zhang, He, & Zhan, 2023) and the long-term trends of the ecosystem (Sauzède et al., 2017). For ecosystem modeling, our method can also provide timely and considerably accurate multiyear initial conditions and boundary constraints for nitrate, better simulating key biogeochemical processes such as nitrogen cycling, productivity, and biodiversity in the ecosystem (Gruber & Galloway, 2008; Xinning Zhang, Ward, & Sigman, 2020). These further applications can be exploited in future studies.

Acknowledgements:

Funding for this research was provided by the Natural Science Foundation of China (NSFC, Grant No. 41906019). This research was also supported by College Students Innovative Entrepreneurial Training Plan Program (Grant No. 202311164).

References

Arteaga, L., Pahlow, M., & Oschlies, A. (2015). Global monthly sea surface nitrate fields estimated from remotely sensed sea surface temperature, chlorophyll, and modeled mixed layer depth. *Geophysical Research Letters, 42*(4), 1130-1138. doi:https://doi.org/10.1002/2014GL062937

Aumont, O., C., E., Tagliabue, A., Bopp, L., & Gehlen, M. (2015). PISCES-v2: an ocean biogeochemical model for carbon and ecosystem studies. *Geoscientific Model Development, 8*(8), 2465-2513.

Bakun, A. (1973). *Coastal upwelling indices, west coast of North America, 1946-71*. Retrieved from Seattle, WA:

Behrenfeld, M. J. (2010). Abandoning Sverdrup's critical depth hypothesis on phytoplankton blooms. *Ecology, 91*(4), 977-989.

Bristow, L. A., Mohr, W., Ahmerkamp, S., & Kuypers, M. M. J. C. B. (2017). Nutrients that limit growth in the ocean. *27*(11), R474-R478.

Chai, F., Johnson, K. S., Claustre, H., Xing, X., Wang, Y., Boss, E., . . . Sutton, A. (2020). Monitoring ocean biogeochemistry with autonomous platforms. *Nature Reviews Earth & Environment, 1*(6), 315-326. doi:10.1038/s43017-020-0053-y

Chen, G., Han, W., Li, Y., & Wang, D. (2016). Interannual Variability of Equatorial Eastern Indian Ocean Upwelling: Local versus Remote Forcing. *Journal of Physical Oceanography, 46*(3), 789-807. doi:10.1175/jpo-d-15-0117.1

Dai, M., Luo, Y.-W., Achterberg, E. P., Browning, T. J., Cai, Y., Cao, Z., . . . Zhou, K. (2023). Upper Ocean Biogeochemistry of the Oligotrophic North Pacific Subtropical Gyre: From Nutrient Sources to Carbon Export. *Reviews of Geophysics, 61*(3), e2022RG000800. doi:https://doi.org/10.1029/2022RG000800

Dai, Y., Cao, L., & Wang, B. (2020). Marine biogeochemical cycling and oceanic CO2 uptake simulated by the NUIST Earth System Model version 3 (NESM v3). *Geosci. Model Dev., 13*(7), 3119-3144. doi:10.5194/gmd-13-3119-2020

Das, D., Chakrabarty, M., Goswami, S., Basu, D., & Chaudhuri, S. (2019). Impact of intra-seasonal oscillations of Indian summer monsoon on biogeochemical constituents of North Indian Ocean. *Theoretical and Applied Climatology, 136*(3), 839-848. doi:10.1007/s00704-018-2518-1

Ding, Y., Chen, Z., Lu, W., & Wang, X. (2021). A CatBoost approach with wavelet decomposition to improve satellite-derived high-resolution PM2.5 estimates in Beijing-Tianjin-Hebei. *Atmospheric Environment, 249*. doi:10.1016/j.atmosenv.2021.118212

Dong, C., Xu, G., Han, G., Bethel, B. J., Xie, W., & Zhou, S. (2022). Recent Developments in Artificial Intelligence in Oceanography. *Ocean-Land-Atmosphere Research, 2022*. doi:doi:10.34133/2022/9870950

Du, C., He, R., Liu, Z., Huang, T., Wang, L., Yuan, Z., . . . Dai, M. (2021). Climatology of nutrient distributions in the South China Sea based on a large data set derived from a new algorithm. *Progress in Oceanography, 195*, 102586.

Fan, F. L., Xiong, J., Li, M., & Wang, G. (2021). On Interpretability of Artificial Neural Networks: A Survey. *IEEE Transactions on Radiation and Plasma Medical Sciences, 5*(6), 741-760. doi:10.1109/TRPMS.2021.3066428

Feng, M., Boschetti, F., Ling, F., Zhang, X., Hartog, J. R., Akhtar, M., . . . Hobday, A. J. (2022). Predictability of sea surface temperature anomalies at the eastern pole of the Indian Ocean Dipole—using a convolutional neural network model. *Frontiers in Climate, 4*. doi:10.3389/fclim.2022.925068

Foster, D., Gagne II, D. J., & Whitt, D. B. (2021). Probabilistic Machine Learning Estimation of Ocean Mixed Layer Depth From Dense Satellite and Sparse In Situ Observations. *Journal of Advances in Modeling Earth Systems, 13*(12), e2021MS002474. doi:https://doi.org/10.1029/2021MS002474

Gao, Z., Shi, X., Wang, H., Zhu, Y., Wang, Y. B., Li, M., & Yeung, D.-Y. (2022). Earthformer: Exploring space-time transformers for earth system forecasting. *Advances in Neural Information Processing Systems, 35*, 25390-25403.

Garcia, H., Boyer, T., Locarnini, R., Baranova, O., & Zweng, M. (2018). World ocean database 2018: User's manual (prerelease). *NOAA Atlas NESDIS81*.

Goes, J. I., Saino, T., Oaku, H., & Jiang, D. L. (1999). A method for estimating sea surface nitrate concentrations from remotely sensed SST and chlorophyll aa case study for the north Pacific Ocean using OCTS/ADEOS data. *IEEE Transactions on Geoscience and Remote Sensing, 37*(3), 1633-1644.

Gruber, N., & Galloway, J. N. (2008). An Earth-system perspective of the global nitrogen cycle. *Nature, 451*(7176), 293-296.

Guieu, C., Aumont, O., Paytan, A., Bopp, L., Law, C. S., Mahowald, N., . . . Völker, C. (2014). The significance of the episodic nature of atmospheric deposition to Low Nutrient Low Chlorophyll regions. *Global Biogeochemical Cycles, 28*(11), 1179-1198. doi:10.1002/2014gb004852

Guinehut, S., Dhomps, A. L., Larnicol, G., & Le Traon, P. Y. (2012). High resolution 3-D temperature and salinity fields derived from in situ and satellite observations. *Ocean Sci., 8*(5), 845-857. doi:10.5194/os-8-845-2012

Ham, Y.-G., Kim, J.-H., & Luo, J.-J. (2019). Deep learning for multi-year ENSO forecasts. *Nature, 573*(7775), 568-572. doi:10.1038/s41586-019-1559-7

Hersbach, H., Bell, B., Berrisford, P., Hirahara, S., Horányi, A., Muñoz-Sabater, J., . . . Thépaut, J. N. (2020). The ERA5 global reanalysis. *Quarterly Journal of the Royal Meteorological Society, 146*(730), 1999-2049. doi:10.1002/qj.3803

Holder, C., & Gnanadesikan, A. (2021). Can machine learning extract the mechanisms controlling phytoplankton growth from large-scale observations? – A proof-of-concept study. *Biogeosciences, 18*(6), 1941-1970. doi:10.5194/bg-18-1941-2021

Holm, E. A. (2019). In defense of the black box. *364*(6435), 26-27. doi:10.1126/science.aax0162 %J Science

Hutchins, D. A., & Capone, D. G. (2022). The marine nitrogen cycle: new developments and global change. *Nature Reviews Microbiology, 20*(7), 401-414. doi:10.1038/s41579-022-00687-z

Karniadakis, G. E., Kevrekidis, I. G., Lu, L., Perdikaris, P., Wang, S., & Yang, L. (2021). Physics-informed machine learning. *Nature Reviews Physics, 3*(6), 422-440. doi:10.1038/s42254-021-00314-5

Keerthi, M. G., Lengaigne, M., Levy, M., Vialard, J., Parvathi, V., de Boyer Montégut, C., . . . Muraleedharan, P. M. (2017). Physical control of interannual variations of the winter chlorophyll bloom in the northern Arabian Sea. *Biogeosciences, 14*(15), 3615-3632. doi:10.5194/bg-14-3615-2017

Klemas, V., & Yan, X.-H. (2014). Subsurface and deeper ocean remote sensing from satellites: An overview and new results. *Progress in Oceanography, 122*(0), 1-9. doi:http://dx.doi.org/10.1016/j.pocean.2013.11.010

Koné, V., Aumont, O., Lévy, M., & Resplandy, L. (2009). Physical and Biogeochemical Controls of the Phytoplankton Seasonal Cycle in the Indian Ocean: A Modeling Study. In *Indian Ocean Biogeochemical Processes and Ecological Variability* (pp. 147-166).

Konya, A., & Nematzadeh, P. (2024). Recent applications of AI to environmental disciplines: A review. *Science of the Total Environment*, *906*, 167705. doi:https://doi.org/10.1016/j.scitotenv.2023.167705

Lahiri, S. P., & Vissa, N. K. (2022). Assessment of Indian Ocean upwelling changes and its relationship with the Indian monsoon. *Global and Planetary Change*, *208*, 103729. doi:https://doi.org/10.1016/j.gloplacha.2021.103729

Lek, S., & Guégan, J. F. (1999). Artificial neural networks as a tool in ecological modelling, an introduction. *Ecological Modelling*, *120*(2), 65-73. doi:https://doi.org/10.1016/S0304-3800(99)00092-7

Li, F., Burger, A., Eppley, J. M., Poff, K. E., Karl, D. M., & DeLong, E. F. (2023). Planktonic microbial signatures of sinking particle export in the open ocean’s interior. *Nat Commun, 14*(1). doi:10.1038/s41467-023-42909-9

Li, X., Liu, B., Zheng, G., Ren, Y., Zhang, S., Liu, Y., . . . Wang, F. (2020). Deep-learning-based information mining from ocean remote-sensing imagery. *National Science Review, 7*(10), 1584-1605. doi:10.1093/nsr/nwaa047

Liu, Y., Lu, W., Wang, D., Lai, Z., Ying, C., Li, X., . . . Dong, C. (2024). Spatiotemporal wave forecast with transformer-based network: A case study for the northwestern Pacific Ocean. *Ocean Modelling*. doi:10.1016/j.ocemod.2024.102323

Lu, W., Oey, L.-Y., Liao, E., Zhuang, W., Yan, X.-H., & Jiang, Y. (2018). Physical modulation to the biological productivity in the summer Vietnam upwelling system. *Ocean Science, 14*(5), 1303-1320. doi:10.5194/os-14-1303-2018

Lu, W., & Su, H. (2023). Ocean Heat Content Retrieval from Remote Sensing Data Based on Machine Learning. In *Artificial Intelligence Oceanography* (pp. 125-145): Springer Nature Singapore Singapore.

Lu, W., Su, H., Yang, X., & Yan, X.-H. (2019). Subsurface temperature estimation from remote sensing data using a clustering-neural network method. *Remote Sensing of Environment, 229*, 213-222.

Lu, Z., Gan, J., Dai, M., Zhao, X., & Hui, C. R. (2020). Nutrient transport and dynamics in the South China Sea: A modeling study. *Progress in Oceanography, 183*. doi:10.1016/j.pocean.2020.102308

Madec, G. (2008). NEMO reference manual, ocean dynamics component: NEMO-OPA. *Note du Pole de modélisation, Institut Pierre-Simon Laplace , France*(27), 1288-1161.

Martinez, E., Brini, A., Gorgues, T., Drumetz, L., Roussillon, J., Tandeo, P., . . . Fablet, R. (2020). Neural Network Approaches to Reconstruct Phytoplankton Time-Series in the Global Ocean. *Remote Sensing, 12*(24). doi:10.3390/rs12244156

Neelin, J. D., Battisti, D. S., Hirst, A. C., Jin, F.-F., Wakata, Y., Yamagata, T., & Zebiak, S. E. (1998). ENSO theory. *Journal of Geophysical Research: Oceans, 103*(C7), 14261-14290. doi:https://doi.org/10.1029/97JC03424

Olsen, A., Key, R. M., van Heuven, S., Lauvset, S. K., Velo, A., Lin, X., . . . Suzuki, T. (2016). The Global Ocean Data Analysis Project version 2 (GLODAPv2) – an internally consistent data product for the world ocean. *Earth Syst. Sci. Data, 8*(2), 297-323. doi:10.5194/essd-8-297-2016

Olsen, A., Lange, N., Key, R. M., Tanhua, T., Bittig, H. C., Kozyr, A., . . . Brown, P. J. J. E. S. S. D. (2020). An updated version of the global interior ocean biogeochemical data product, GLODAPv2. 2020. *12*(4), 3653-3678.

Park, J., Lee, W. H., Kim, K. T., Park, C. Y., Lee, S., & Heo, T.-Y. (2022). Interpretation of ensemble learning to predict water quality using explainable artificial intelligence. *Science of the Total Environment, 832,* 155070. doi:https://doi.org/10.1016/j.scitotenv.2022.155070

Person, R., Aumont, O., Madec, G., Vancoppenolle, M., Bopp, L., & Merino, N. (2019). Sensitivity of ocean biogeochemistry to the iron supply from the Antarctic Ice Sheet explored with a biogeochemical model. *Biogeosciences, 16*(18), 3583-3603. doi:10.5194/bg-16-3583-2019

Portillo Juan, N., Matutano, C., & Negro Valdecantos, V. (2023). Uncertainties in the application of artificial neural networks in ocean engineering. *Ocean Engineering, 284*, 115193. doi:https://doi.org/10.1016/j.oceaneng.2023.115193

Prechelt, L. (2012). Early Stopping — But When? In G. Montavon, G. B. Orr, & K.-R. Müller (Eds.), *Neural Networks: Tricks of the Trade: Second Edition* (pp. 53-67). Berlin, Heidelberg: Springer Berlin Heidelberg.

Raddatz, J., Beisel, E., Butzin, M., Schröder-Ritzrau, A., Betzler, C., Friedrich, R., & Frank, N. (2023). Variable ventilation ages in the equatorial Indian Ocean thermocline during the LGM. *Scientific Reports, 13*(1), 11355. doi:10.1038/s41598-023-38388-z

Raissi, M., Perdikaris, P., & Karniadakis, G. E. (2019). Physics-informed neural networks: A deep learning framework for solving forward and inverse problems involving nonlinear partial differential equations. *Journal of Computational Physics, 378*, 686-707. doi:https://doi.org/10.1016/j.jcp.2018.10.045

Reichstein, M., Camps-Valls, G., Stevens, B., Jung, M., Denzler, J., Carvalhais, N., & Prabhat. (2019). Deep learning and process understanding for data-driven Earth system science. *Nature, 566*(7743), 195-204. doi:10.1038/s41586-019-0912-1

Rixen, T., Gaye, B., & Emeis, K.-C. (2019). The monsoon, carbon fluxes, and the organic carbon pump in the northern Indian Ocean. *Progress in Oceanography, 175*, 24-39. doi:https://doi.org/10.1016/j.pocean.2019.03.001

Ronneberger, O., Fischer, P., & Brox, T. (2015). *U-net: Convolutional networks for biomedical image segmentation.* Paper presented at the Medical Image Computing and Computer-Assisted Intervention–MICCAI 2015: 18th International Conference, Munich, Germany, October 5-9, 2015, Proceedings, Part III 18.

Saida, S. J., & Ari, S. (2022). MU-Net: Modified U-Net Architecture for Automatic Ocean Eddy Detection. *IEEE Geoscience and Remote Sensing Letters, 19*, 1-5. doi:10.1109/LGRS.2022.3225140

Samek, W., Montavon, G., Lapuschkin, S., Anders, C. J., & Müller, K. R. (2021). Explaining Deep Neural Networks and Beyond: A Review of Methods and Applications. *Proceedings of the IEEE, 109*(3), 247-278. doi:10.1109/JPROC.2021.3060483

Sarma, V. V. S. S., Bhaskar, T. V. S. U., Kumar, J. P., & Chakraborty, K. (2020). Potential mechanisms responsible for occurrence of core oxygen minimum zone in the north-eastern Arabian Sea. *Deep Sea Research Part I: Oceanographic Research Papers, 165*, 103393. doi:https://doi.org/10.1016/j.dsr.2020.103393

Sauzède, R., Bittig, H. C., Claustre, H., Pasqueron de Fommervault, O., Gattuso, J.-P., Legendre, L., & Johnson, K. S. (2017). Estimates of water-column nutrient concentrations and carbonate system parameters in the global ocean: A novel approach based on neural networks. *Frontiers in Marine Science, 4*, 128.

Schott, F. A., & McCreary, J. P. (2001). The monsoon circulation of the Indian Ocean. *Progress in Oceanography, 51*(1), 1-123. doi:https://doi.org/10.1016/S0079-6611(01)00083-0

Schwendike, J., Berry, G. J., Reeder, M. J., Jakob, C., Govekar, P., & Wardle, R. (2015). Trends in the local Hadley and local Walker circulations. *Journal of Geophysical Research: Atmospheres, 120*(15), 7599-7618. doi:https://doi.org/10.1002/2014JD022652

Seelanki, V., Nigam, T., & Pant, V. (2022). Unravelling the roles of Indian Ocean Dipole and El-Niño on winter primary productivity over the Arabian Sea. *Deep Sea Research Part I: Oceanographic Research Papers, 190*, 103913. doi:https://doi.org/10.1016/j.dsr.2022.103913

Shafeeque, M., Shah, P., Platt, T., Sathyendranath, S., Menon, N. N., Balchand, A. N., & George, G. (2019). Effect of Precipitation on Chlorophyll-a in an Upwelling Dominated Region Along the West Coast of India. *Journal of Coastal Research, 86*(sp1), 218-224, 217. Retrieved from https://doi.org/10.2112/SI86-032.1

Shcherbakov, M., Brebels, A., Shcherbakova, N. L., Tyukov, A., Janovsky, T. A., & Kamaev, V. A. (2013). A survey of forecast error measures. *World Applied Sciences Journal, 24*, 171-176. doi:10.5829/idosi.wasj.2013.24.itmies.80032

Singh, A., Gandhi, N., & Ramesh, R. (2012). Contribution of atmospheric nitrogen deposition to new production in the nitrogen limited photic zone of the northern Indian Ocean. *Journal of Geophysical Research: Oceans, 117*(C6). doi:https://doi.org/10.1029/2011JC007737

Singh, A., & Ramesh, R. (2015). Environmental controls on new and primary production in the northern Indian Ocean. *Progress in Oceanography, 131*, 138-145. doi:https://doi.org/10.1016/j.pocean.2014.12.006

Siswanto, S., & Suratno. (2008). Seasonal pattern of wind induced upwelling over Java - Bali Sea waters and surrounding area. *Int J Remote Sens Earth Sci, 5*, 46-56.

Sonnewald, M., Lguensat, R., Jones, D. C., Dueben, P. D., Brajard, J., & Balaji, V. (2021). Bridging observations, theory and numerical simulation of the ocean using machine learning. *Environmental Research Letters, 16*(7), 073008. doi:10.1088/1748-9326/ac0eb0

Su, H., Jiang, J., Wang, A., Zhuang, W., & Yan, X.-H. (2022). Subsurface Temperature Reconstruction for the Global Ocean from 1993 to 2020 Using Satellite Observations and Deep Learning. *Remote Sensing, 14*(13). doi:10.3390/rs14133198

Su, H., Lu, X., Chen, Z., Zhang, H., Lu, W., & Wu, W. (2021). Estimating Coastal Chlorophyll-A Concentration from Time-Series OLCI Data Based on Machine Learning. *Remote Sensing, 13*(4). doi:10.3390/rs13040576

Su, H., Wei, Y., Lu, W., Yan, X.-H., & Zhang, H. (2023). Unabated Global Ocean Warming Revealed by Ocean Heat Content from Remote Sensing Reconstruction. *Remote Sensing, 15*(3). doi:10.3390/rs15030566

Su, H., Zhang, T., Lin, M., Lu, W., & Yan, X.-H. (2021). Predicting subsurface thermohaline structure from remote sensing data based on long short-term memory neural networks. *Remote Sensing of Environment, 260*, 112465. doi:https://doi.org/10.1016/j.rse.2021.112465

Sun, N., Zhou, Z., Li, Q., & Zhou, X. (2022). Spatiotemporal Prediction of Monthly Sea Subsurface Temperature Fields Using a 3D U-Net-Based Model. *Remote Sensing, 14*(19), 4890. Retrieved from https://www.mdpi.com/2072-4292/14/19/4890

Sundararajan, M., Taly, A., & Yan, Q. (2017). *Axiomatic attribution for deep networks.* Paper presented at the International conference on machine learning.

Susanto, R. D., Gordon, A. L., & Zheng, Q. (2001). Upwelling along the coasts of Java and Sumatra and its relation to ENSO. *Geophysical Research Letters, 28*(8), 1599-1602. doi:10.1029/2000gl011844

Tagliabue, A. (2023). ‘Oceans are hugely complex’: modelling marine microbes is key to climate forecasts. *Nature, 623*(7986), 250-252.

Talley, L. D., Feely, R. A., Sloyan, B. M., Wanninkhof, R., Baringer, M. O., Bullister, J. L., . . . Zhang, J. Z. (2016). Changes in Ocean Heat, Carbon Content, and Ventilation: A Review of the First Decade of GO-SHIP Global Repeat Hydrography. *Annual review of marine science, 8*(1), 185-215. doi:10.1146/annurev-marine-052915-100829

Taylor, J., & Feng, M. (2022). A deep learning model for forecasting global monthly mean sea surface temperature anomalies. *Frontiers in Climate, 4*. doi:10.3389/fclim.2022.932932

Tokinaga, H., & Tanimoto, Y. (2004). Seasonal Transition of SST Anomalies in the Tropical Indian Ocean during El Niño and Indian Ocean Dipole Years. *Journal of the Meteorological Society of Japan. Ser. II, 82*(4), 1007-1018. doi:10.2151/jmsj.2004.1007

Voss, M., Bange, H. W., Dippner, J. W., Middelburg, J. J., Montoya, J. P., & Ward, B. (2013). The marine nitrogen cycle: recent discoveries, uncertainties and the potential relevance of climate change. *Philosophical Transactions of the Royal Society B: Biological Sciences, 368*(1621), 20130121. doi:10.1098/rstb.2013.0121

Wahyudi, A. a. J., Triana, K., Masumoto, Y., Rachman, A., Firdaus, M. R., Iskandar, I., & Meirinawati, H. (2023). Carbon and nutrient enrichment potential of South Java upwelling area as detected using hindcast biogeochemistry variables. *Regional Studies in Marine Science, 59*, 102802. doi:https://doi.org/10.1016/j.rsma.2022.102802

Wang, L., Xu, Z., Gong, X., Zhang, P., Hao, Z., You, J., . . . Guo, X. (2023). Estimation of nitrate concentration and its distribution in the northwestern Pacific Ocean by a deep neural network model. *Deep Sea Research Part I: Oceanographic Research Papers, 195*, 104005.

Wang, T., Yu, P., Wu, Z., Lu, W., Liu, X., Li, Q. P., & Huang, B. (2021). Revisiting the Intraseasonal Variability of Chlorophyll-a in the Adjacent Luzon Strait With a New Gap-Filled Remote Sensing Data Set. *IEEE Transactions on Geoscience and Remote Sensing, 60*, 1-11. doi:10.1109/tgrs.2021.3067646

Wyrtki, K. (1973). An equatorial jet in the Indian Ocean. *Science, 181*(4096), 262-264.

Xie, H., Xu, Q., Cheng, Y., Yin, X., & Fan, K. (2023). Reconstructing three-dimensional salinity field of the South China Sea from satellite observations. *Frontiers in Marine Science, 10*. doi:10.3389/fmars.2023.1168486

Xie, H., Xu, Q., Cheng, Y., Yin, X., & Jia, Y. (2022). Reconstruction of Subsurface Temperature Field in the South China Sea From Satellite Observations Based on an Attention U-Net Model. *IEEE Transactions on Geoscience and Remote Sensing, 60*, 1-19. doi:10.1109/TGRS.2022.3200545

Xu, T., Wei, Z., Susanto, R., Li, S., Wang, Y., Wang, Y., . . . Sulistyo, B. (2021). Observed water exchange between the South China Sea and Java Sea through Karimata strait. *Journal of Geophysical Research: Oceans, 126*(2), e2020JC016608.

Zhan, W., Zhang, Y., He, Q., & Zhan, H. (2023). Shifting responses of phytoplankton to atmospheric and oceanic forcing in a prolonged marine heatwave. *Limnology and Oceanography*.

Zhang, K., Geng, X., & Yan, X.-H. (2020). Prediction of 3-D ocean temperature by multilayer convolutional LSTM. *IEEE Geoscience and Remote Sensing Letters, 17*(8), 1303-1307.

Zhang, X., Ward, B. B., & Sigman, D. M. (2020). Global nitrogen cycle: critical enzymes, organisms, and processes for nitrogen budgets and dynamics. *Chemical reviews, 120*(12), 5308-5351.

Zhang, X., Zhao, N., & Han, Z. (2023). A Modified U-Net Model for Predicting the Sea Surface Salinity over the Western Pacific Ocean. *Remote Sensing, 15*(6), 1684. Retrieved from https://www.mdpi.com/2072-4292/15/6/1684

Zhao, N., Huang, B., Yang, J., Radenkovic, M., & Chen, G. (2023). Oceanic Eddy Identification Using Pyramid Split Attention U-Net With Remote Sensing Imagery. *IEEE Geoscience and Remote Sensing Letters, 20*, 1-5. doi:10.1109/LGRS.2023.3243902

Zhou, Y., Lu, C., Chen, K., & Li, X. (2023). Sea Surface Height Anomaly Prediction Based on Artificial Intelligence. In X. Li & F. Wang (Eds.), *Artificial Intelligence Oceanography* (pp. 63-82). Singapore: Springer Nature Singapore.

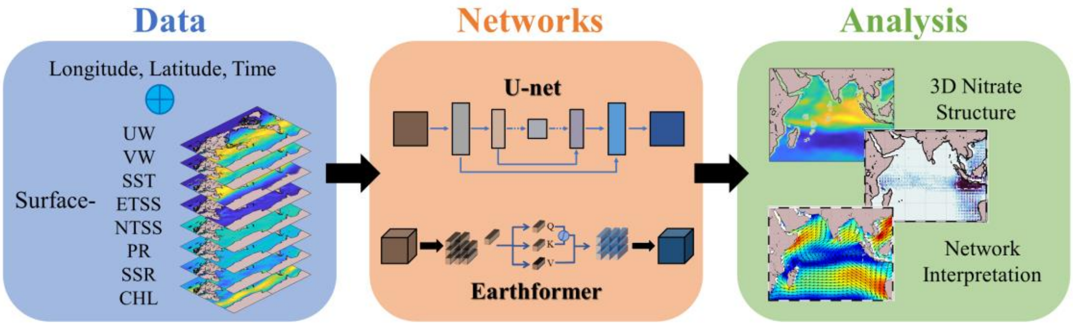

Graphical abstract

Highlights for:

Can Three-dimensional Nitrate Structure be Reconstructed from Surface Information with Artificial Intelligence? – A Proof-of-concept Study

Guangyu Gary Yang[1], Qishuo Wang[1], Jiacheng Feng[1], Lechi He[1], Rongzu Li[1],
Wenfang Lu[1, 2,]*, Enhui Liao[3], Zhigang Lai[1, 2]

[1] School of Marine Sciences, Sun Yat-Sen University, Zhuhai, Guangdong, China

[2] Southern Marine Science and Engineering Guangdong Laboratory (Zhuhai), Zhuhai, 519000, China

[3] School of Oceanography, Shanghai Jiao Tong University, Shanghai, 200030, China

*** Corresponding author:**
Wenfang Lu
luwf6@sysu.edu.cn

Highlights:

- Two advanced AI networks were applied in reconstructing 3D structure of nitrate from surface data
- A deep learning interpretation technique was used to explain the spatio-temporal influence of each input feature
- Networks can achieve high accuracy and capture interannual nitrate anomalies, reflecting its dynamic control